OPTICS

Electrically addressable integrated intelligent terahertz metasurface

Benwen Chen[1], Xinru Wang[2], Weili Li[1], Chun Li[1], Zhaosong Wang[1], Hangbin Guo[1], Jingbo Wu[1,3]*, Kebin Fan[1,3], Caihong Zhang[1,3], Yunbin He[2], Biaobing Jin[1,3]*, Jian Chen[1,3], Peiheng Wu[1]

Reconfigurable intelligent surfaces (RISs) play an essential role in various applications, such as next-generation communication, uncrewed vehicles, and vital sign recognizers. However, in the terahertz (THz) region, the development of RISs is limited because of lacking tunable phase shifters and low-cost sensors. Here, we developed an integrated self-adaptive metasurface (SAM) with THz wave detection and modulation capabilities based on the phase change material. By applying various coding sequences, the metasurface could deflect THz beams over an angle range of 42.8°. We established a software-defined sensing reaction system for intelligent THz wave manipulation. In the system, the SAM self-adaptively adjusted the THz beam deflection angle and stabilized the reflected power in response to the detected signal without human intervention, showing vast potential in eliminating coverage dead zones and other applications in THz communication. Our programmable controlled SAM creates a platform for intelligent electromagnetic information processing in the THz regime.

INTRODUCTION

With the development of next-generation wireless communication, there is a booming need for intelligent beamforming and electromagnetic signal processing (*1–3*). The emergent reconfigurable intelligent surfaces (RISs) provide a promising solution for reconfiguring the electromagnetic wave propagation environment by controlling the complex reflection coefficients of their elements (*4*). For example, by controlling the surface phase profile, RIS can function as a low-cost passive phased array for beamforming, which is essential to improving the link at the dead zone and suppress the cochannel interference at the cell edges. Besides that, RISs have other potential applications in wireless communication, such as physical layer security enhancement and signal hot spot creation (*5–7*).

The realization of RISs at microwave frequencies is based on programmable metasurfaces, which typically comprise a planar array of meta-atoms integrated with electronic switches (*8, 9*). In recent years, intelligent metasurfaces have been proposed as an upgraded version of the programmable metasurface (*10–12*). By combining sensors into the programmable metasurface, intelligent metasurfaces that can adjust their functionality according to the surrounding environment have been created. Intelligent metasurfaces, especially those enhanced by artificial intelligence algorithms, have exhibited powerful capability in the flexible manipulation of electromagnetic waves, as demonstrated by self-adaptive cloaking, intelligent beam steering, and monitoring vital signs (*13–18*). Because of technical limitations, most current intelligent metasurfaces work in microwave frequencies. Intelligent metasurfaces in terahertz (THz) and higher frequency bands remain to be developed.

The rich spectral resources available at THz frequencies can substantially enhance the data rate of wireless communication (*19*). A beamforming technique that can self-adaptively focus THz signals to the desired direction is highly demanded to compensate for the severe path loss of THz waves. However, extending the phased array and programmable metasurfaces from microwave to THz frequencies encounters technological challenges due to the lack of electronic switches. In the THz regime, programmable metasurfaces that embed tunable materials, such as semiconductors (*20, 21*), phase transition materials (*22–25*), liquid crystals (*26–30*), and graphene (*31, 32*), into subwavelength resonators, have been implemented. Despite the impressive progress, the major obstacle to realizing THz intelligent metasurfaces is the scarcity of low-cost sensors and pixelated phase modulators (*33*).

Many tunable materials at THz frequencies could be used for sensitive detectors and modulators (*21, 34–39*), which offers a possibility of monolithic integration of low-cost THz sensors and pixelated metasurfaces. Intrigued by this idea, we developed a self-adaptive metasurface (SAM) at THz frequencies using the tremendous conductivity change of vanadium dioxide (VO_2) in the insulator-metal transition (IMT) region (*40*). The SAM can sense the THz environment and steer the reflected THz beams by alternating spatial phase distributions. Then, we constructed an uncrewed sensing-reaction system. The SAM detected the incident THz wave and steered the THz beam self-adaptively with predefined software in the host computer. Furthermore, we conducted two proof-of-concept demonstrations. The experimental results show that the SAM can sense and manipulate THz waves without human intervention. We believe that the concept of SAMs offers a general solution for intelligent metasurfaces at THz and higher frequencies, which potentially have vast applications in communication and other information technologies.

RESULTS

Design of THz SAM and sensing-reaction system

A sketch of a sensing-reaction system based on the SAM is shown in Fig. 1. The SAM is a linear array with 48 subarrays. The reflection coefficient of each subarray can be controlled independently by applying different electrical biases V_i (the subscript i denotes the i-th subarray). Sharp changes in the electrical resistance of VO_2 in the IMT region can be used for sensitive THz detection. Therefore,

[1]Research Institute of Superconductor Electronics (RISE), School of Electronic Science and Engineering, Nanjing University, Nanjing 210023, China. [2]Ministry-of-Education Key Laboratory for the Green Preparation and Application of Functional Materials, Hubei Key Laboratory of Polymer Materials, School of Materials Science and Engineering, Hubei University, Wuhan 430062, China. [3]Purple Mountain Laboratories, Nanjing 211111, China.
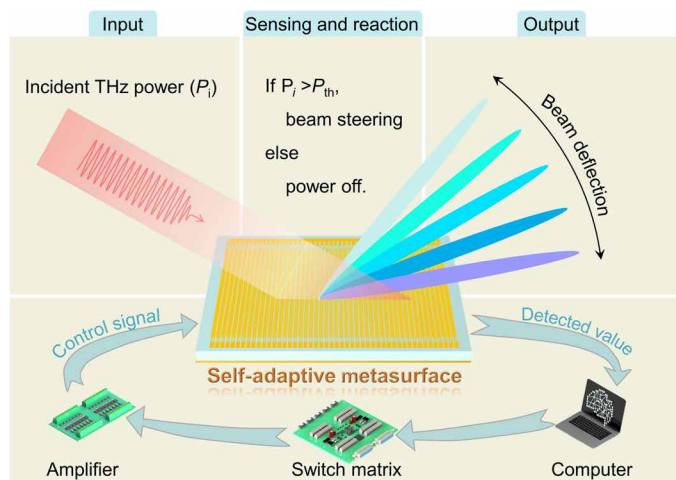*Corresponding author. Email: jbwu@nju.edu.cn (J.W.); bbjin@nju.edu.cn (B.J.)

Fig. 1. Illustration of the VO₂-based THz SAM for self-adaptive beam steering. The metasurface comprises 1×48 subarrays, and each subarray functioned as both a THz reflective modulator and microbolometer under the appropriate bias. The sensing reaction system includes the SAM, a programmable switch matrix, a multichannel power amplifier, and a computer loaded with predefined algorithms. Initially, the SAM detects the power reaching the metasurface (P_i). When the received power is higher than P_{th}, the SAM starts deflecting the THz beam to the predefined direction.

the SAM can simultaneously function as a phased array for THz beam steering and a sensor array. The SAM, a programmable switch matrix, a multichannel power amplifier, and a computer loaded with predefined programs form an intelligent sensing reaction system that can self-adaptively react to changes in the incident wave. Figure 1 illustrates the use of the SAM in self-adaptive THz beam steering without manual instructions. Initially, the SAM detects the THz wave incident to the surface. When the received THz power (P_i) is higher than the threshold power (P_{th}), the SAM starts deflecting the THz beam to the predefined direction.

The structure diagram of the SAM is illustrated in Fig. 2A. For each subarray, one end shares a ground electrode, and the other is connected to an external voltage source (V_i) for independent control. The distance between the adjacent subarrays is 400 μm, approximately 0.57λ, where λ is the free space wavelength at the working frequency of 0.425 THz. Each subarray is composed of 90 rows and two columns of unit cells. To improve the responsivity of the SAM as a microbolometer, we need to reduce the volume of VO₂ patches integrated into the unit cell as much as possible according to the equation of responsivity $R = I_b R_u \alpha \eta / \sqrt{G^2 + \omega^2 C^2}$ (41), where I_b is the bias current, R_u is the resistance of a unit cell, α is the temperature coefficients of resistance, η is the absorption efficiency, G is the thermal conductance, ω is the modulation frequency, and C is the heat capacity of VO₂ materials. Hence, by reducing the volume of VO₂ patches, C can be further decreased, leading to a higher responsivity. Meanwhile, we used a metallic ground to enhance the retroreflection and bowtie antennas to enhance the electric field on the feed gap where the VO₂ microbridge is located. Therefore, as shown in Fig. 2B, each unit cell has a metal-insulator-metal structure. The bottom layer is the metallic ground. Periodic bowtie antennas connected to VO₂ microbridges form the top layer. A 160-μm-thick c-cut sapphire substrate separates these two layers. The inset in Fig. 2B is the close-up of the VO₂ microbridge.

When the external bias is applied, the voltage-induced Joule heat will induce the IMT of the VO₂ microbridges. The simulated reflection amplitude and phase for various VO₂ conductivities are shown in Fig. 2 (C and D). There are three typical states, namely, the OFF, intermediate (IM), and ON states. The corresponding conductivities are 6×10^3, 4×10^4, and 2.5×10^5 S/m, respectively. As VO₂ goes through the phase transition from an insulating (OFF) state to a metallic state (ON), the resonant frequency shifts from 0.425 to 0.507 THz (Fig. 2C), leading to a sharp change in the reflection phase (Fig. 2D). At 0.425 THz, the amplitude of the OFF and ON states are almost the same, and their phase difference is 180°. Thus, a one-bit coding metasurface is achieved. When different voltage biases are applied, the reflection phase of 0° (element "0") or 180° (element "1") could be dynamically switched, resulting in the deflection of the THz beam to a specific angle.

The transmission line method (TLM) is used to analyze the electromagnetic response of each unit cell. An resistor-inductor-capacitor (RLC) series circuit replaces the active layer in the equivalent circuit (42, 43). Fitted curves are shown by the dashed lines in Fig. 2 (C and D). The fitting parameters of R, L, and C extracted from the simulated reflection spectra for the OFF and ON states are shown in Fig. 2B. The increased L in the metallic state mainly causes the shift in resonance frequency. A near-perfect absorption is achieved in the IM state (blue) at 0.425 THz. As shown in Fig. 2E, the electric field is enhanced in the region of VO₂, indicating that most of the incident power at the absorption frequency is captured by the VO₂ microbridge. Therefore, the structure is favorable for a microbolometer with high responsivity.

However, before applying coding sequences to alter the phase distribution of the SAM for beam deflection, we should first address thermal cross-talk between adjacent subarrays as it can deteriorate beam steering performance by obscuring the coding pattern. The thermal contact between the metasurface and hot plate is crucial for suppressing the thermal cross-talk (24). Here, we use a thermal paste with a conductivity of 14.3 W/(m·K) to decrease the thermal resistance and suppress the lateral thermal diffusion. The simulated cross-sectional temperature distribution for different thermal conductivities of thermal paste is depicted in Fig. 2 (F and G). The results are obtained when the temperatures of the active layer and hot plate are 68° and 60°C, respectively. We plot the corresponding temperature distribution at $z = 0$ for comparison in Fig. 2H. The results show that the thermal paste with high thermal conductivity leads to excellent suppression of the thermal cross-talk.

Performance of THz beam deflection and detection
We fabricated the proposed SAM using the microfabrication process (see Materials and Methods and section S1 for details) and experimentally characterized its performance. A photograph of the fabricated sample on a printed circuit board is shown in Fig. 3A. We electrically controlled the SAM by applying different voltage configurations. The corresponding coding sequences determined the deflection angle of the THz beam. For example, for a coding sequence of /0011…/ (denoted by P4; see Fig. 3B), the element of 1 was realized by applying a high voltage of 20 V (V_{ON}), whereas the rest were biased at a low voltage ($V_{OFF} = 0$ V). According to the generalized Snell's law and the theory of antenna arrays (44, 45), the angle of deflected beam can be described by the following

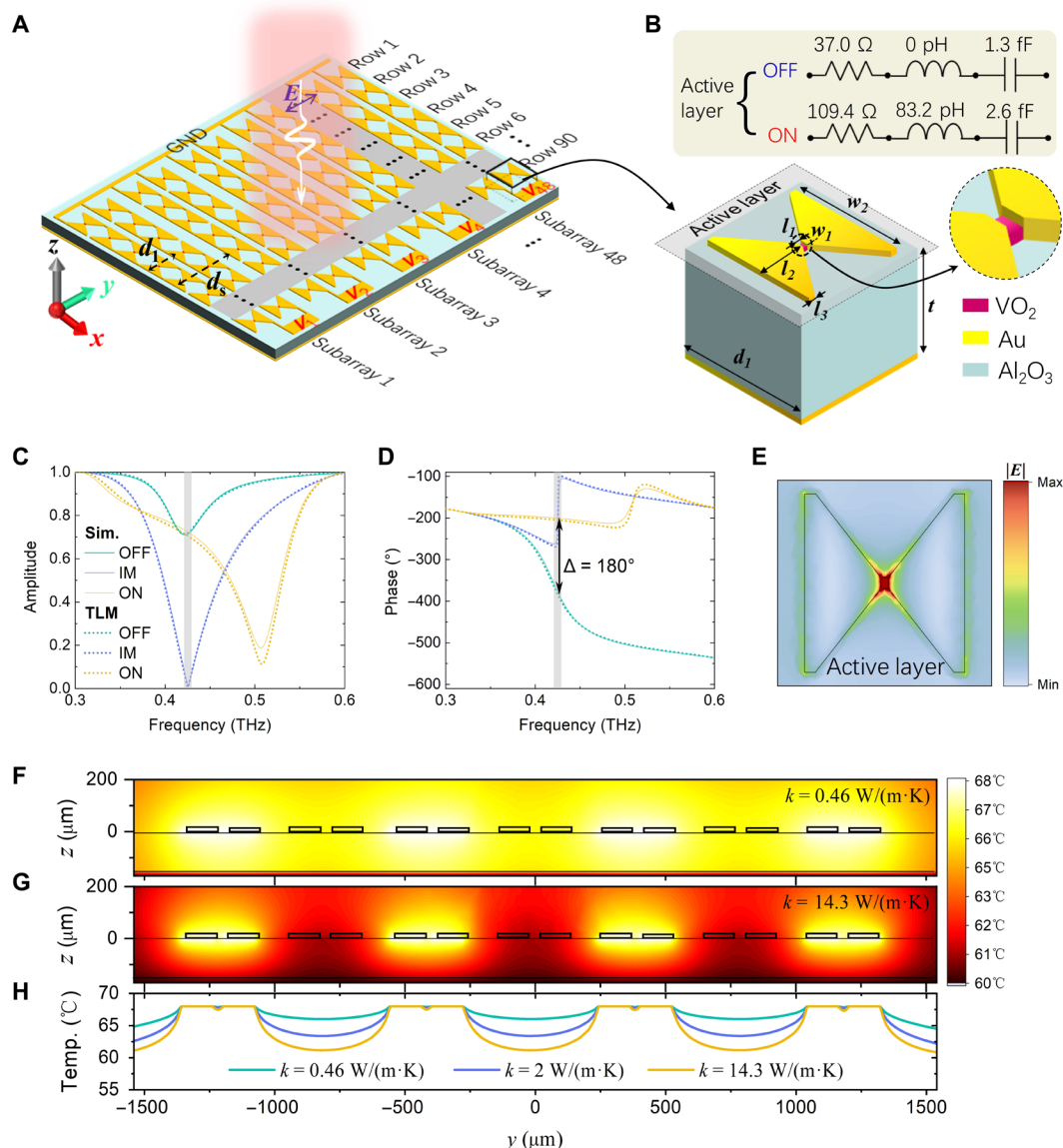$$|\sin\theta_r - \sin\theta_i| = \frac{l\lambda}{M d_s}, (l = 0, \pm1, \pm2, \pm3\ldots) \quad (1)$$

Fig. 2. Structural design and thermal management of the SAM. (**A**) Schematic diagram of the SAM. One end is connected to an external bias (V_i) for individually controlling each subarray, and the other is connected to a common electrical ground (GND). The period of subarrays along the y direction (d_s) is 400 μm. (**B**) Schematic diagram of a unit cell in the SAM. The geometric parameters are set as follows: $w_1 = 8$ μm, $l_1 = 5$ μm, $l_2 = 57.5$ μm, $w_2 = 140$ μm, $l_3 = 8$ μm, $d_1 = 160$ μm, and $t = 160$ μm. The top layer comprises VO_2 microbridges and bowtie antennas. The equivalent RLC series circuit parameters of the active layer in the insulating (OFF) and metallic (ON) states are extracted by fitting the simulated curves. The inset shows the close-up of the VO_2 microbridge. (**C** and **D**) Simulated reflection amplitude (C) and phase (D) spectra of the periodic unit cells for an incident y-polarized THz wave when VO_2 is in the OFF ($\sigma = 6000$ S/m), IM ($\sigma = 40000$ S/m), and ON ($\sigma = 250000$ S/m) states. The solid curves are the simulation results, whereas the dashed lines are the fitted curves based on transmission line theory. (**E**) Electric field distribution of $f = 0.425$ THz on the active layer when VO_2 is in the IM state with $\sigma = 40000$ S/m. (**F** and **G**) Temperature distribution in the yOz cross section of the SAM with different thermal conductivities of the thermally conductive layer when VO_2 is at a transition temperature of 68°C. Conductive silicone grease with $k = 14.3$ W/(m·K) is used for the thermally conductive layer. (**H**) Temperature distribution along the line at $z = 0$ for three cases.

where θ_r is the deflection angle, M is the periodicity of the pattern in terms of the subarray number, and d_s is the width of each subarray as illustrated in Fig. 2A. For example, for a metasurface with a coding sequence of /010011…/ (P3), M of the coding sequence is 6. The deflection angles of the two main reflected beams relative to the specular reflection angle were 18.5° and 42.8° (as shown in the "P3" of Fig. 3C, in which θ_r is denoted by the angle difference relative to the specular reflection, i.e., $\Delta\theta = \theta_r - \theta_{sp}$), corresponding to $l = 1$ and $l = 2$, respectively (see detailed analysis in Materials and Methods).

The measured angular distribution of the deflected beam with various coding sequences sketched in Fig. 3B is shown in Fig. 3C. The electric field is normalized to the largest deflected field scattered by the SAM with a coding sequence of /0000…/. When we switched the coding sequences, the phase gradient varied, resulting in a change in the deflection angle. From Fig. 3C, the maximum deflection angle of the proposed SAM was 42.8°. For comparison, we calculated the corresponding angular distribution pattern based on phased array theory, and the numerical results are also shown (gray lines)
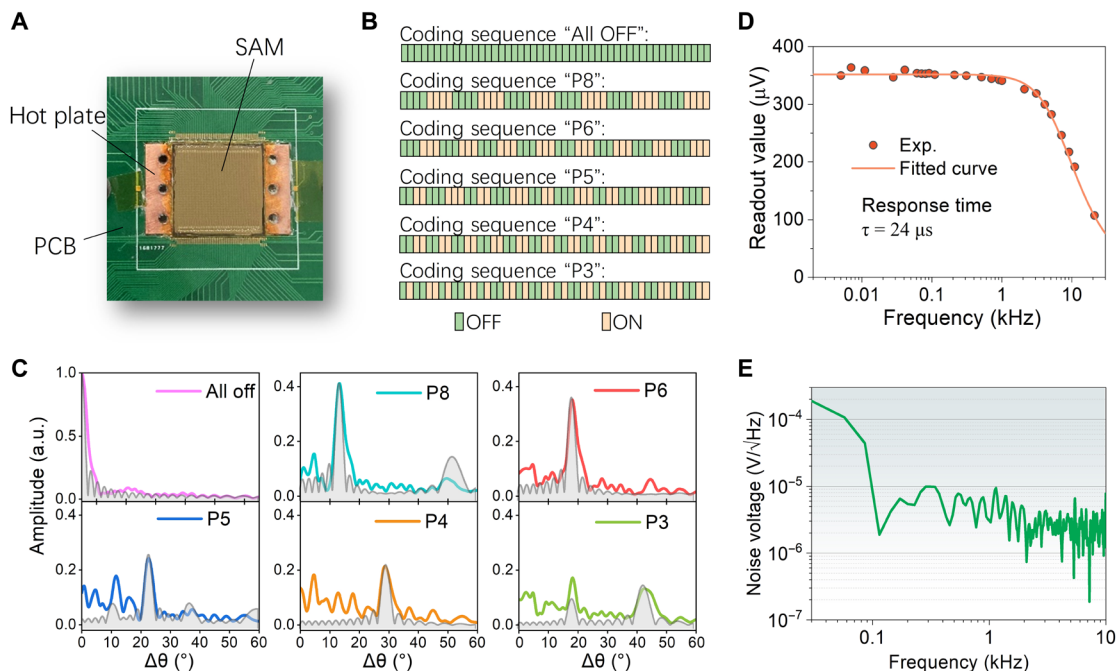
Fig. 3. Performance of THz beam steering and detection of the SAM. (**A**) Photograph of the fabricated SAM loaded on a printed circuit board (PCB). (**B**) Coding sequences used for beam deflection; OFF denotes the subarray is in the OFF state with $V_{OFF} = 0$ V, while ON represents that the subarray is in the ON state with $V_{ON} = 20$ V. (**C**) Measured (colored lines) and calculated (gray lines) angle distributions of the reflected field at 0.425 THz for various coding sequences with an incident angle of 15°; $\Delta\theta$ is the angle relative to the specular angle, i.e., $\Delta\theta = \theta_r - \theta_{sp}$, where θ_{sp} is the specular angle. a.u., arbitrary units. (**D**) Measured frequency response (red circle) of the sensor subarray and the fitted curve (solid line) at a biased current of 4 mA and 60°C. (**E**) Measured voltage noise spectra of the sensor subarray.

in Fig. 3C. For comparison, the numerical field amplitudes have been adjusted to the corresponding experimental results so that the amplitude of the main beam is the same. The measured deflection efficiency for the coding sequence of P8 is 7.3%. Although the deflection efficiency for different coding sequences differs, the deflected angles agree well with the calculated results. The difference in amplitudes of the main deflected beam with varying coding sequences can be attributed to the variation of the radiation amplitudes of the metasurface elements with angle.

Next, to verify the capability of the SAM to detect THz waves, we measured its response under THz radiation (see fig. S3A for the experimental setup). Figure 3D shows the relationship between the response voltage and the modulation frequency when the subarray is biased with 4 mA at 60°C. We fitted the experimental data as a function of the modulation frequency to obtain the response time (*46*). The best fit corresponds to a thermal relaxation time of 24 µs. We also measured the responsivity (*R*) of the subarray at a modulation frequency of 3.1 kHz, which was 13.6 V/W (see details in Materials and Methods). As seen in Fig. 3E, we measured the voltage noise spectral density (V_{noise}) of the subarray for THz wave detection. According to the noise equivalent power (NEP) definition, i.e., NEP = V_{noise}/R, the calculated NEP was 2.9×10^{-7} W·Hz$^{-1/2}$.

Intelligent THz beam steering using THz sensing reaction system

Since the proposed SAM can sense and manipulate the incident wave, it can control electromagnetic waves adaptively on the basis of predefined software without manual involvement. In the following section, we present two demonstrations showing the potential application of the proposed SAM in THz communication.

In the first scenario, the SAM is proposed to eliminate the coverage dead zones after detecting the THz signal. We chose one subarray in the middle as the sensor subarray (see section S2). It is biased with a current of 4 mA for THz detection. The voltage response (V_{sense}) is demodulated and sent to the host computer as the sensing signal. When V_{sense} is higher than the predefined threshold voltage (V_{th}), the host computer determines that the THz wave has reached the SAM and sends a command to the programmable switch matrix. Correspondingly, the coding sequence is applied to the other subarrays (modulation subarrays) for beam steering. The voltage sequences control the deflection of the THz wave to a specific angle. In this case, the SAM is working in beam steering (BS) mode (Fig. 4A). When V_{sense} is smaller than the predefined V_{th}, the SAM determines no incident wave. In that case, the SAM goes into power saving (PS) mode (Fig. 4B), and the voltage bias of all the modulation subarrays is removed. The power consumption is correspondingly saved.

As shown in Fig. 4A, to verify whether the SAM can deflect a THz beam to the designed direction ($\theta_r = 28.6°$) after detecting the signal, we placed an external THz detector in the designed direction. The detector can be regarded as a user in a coverage dead zone due to the occlusion of trees or tall buildings. The "OFF" and "ON" states of THz wave incidence were simulated by inserting or removing a metallic baffle in the THz transmission path of SAM. A timing diagram of these two states is shown in the top inset of Fig. 4C. Figure 4C shows the signals detected by the SAM and the external detector when the two states change alternately (see movie S1). When the incident THz wave is blocked, V_{sense} is lower than the V_{th}. The system then determines that there is no incident wave. Correspondingly, the bias of modulation subarrays is turned off for energy saving. However, when the V_{sense} is larger than the V_{th}, the SAM is applied
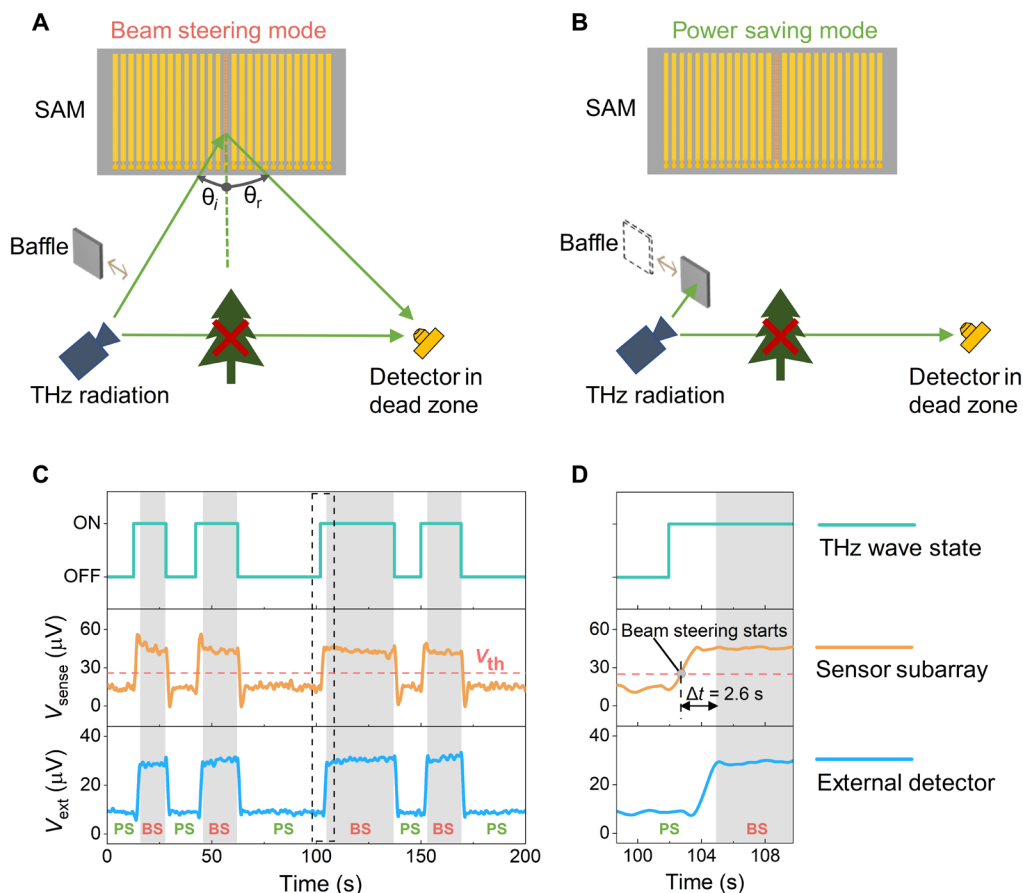
Fig. 4. Proof-of-concept demonstration of self-adaptive beam steering. (**A** and **B**) Schematic of proposed SAM in beam steering mode (A) and power saving mode (B). The collimated THz beam impinges on the SAM at an incident angle of $\theta_i = 15°$. The THz wave reflected by the SAM is received by an external THz detector, which is assumed to be placed in a dead zone caused by trees blocking in a THz communication scenario. The THz beam is deflected to the designed angle of θ_r. For THz sensing, the sensor subarray (red) in the SAM is biased with a current of 4 mA at 60°C. In this case, the SAM is working in beam steering mode. When the incident THz wave is blocked with the metal baffle, the SAM switches to power saving mode. (**C**) Measured signals from the sensor subarray of SAM (orange) and the external THz detector (blue) when the incident THz wave (cyan) is changed between ON and OFF states alternatively. When the readout of the sensor subarray is higher than V_{th}, the SAM begins steering the THz beam under the control of the host computer, and the THz beam is successfully deflected to the direction of θ_r. (**D**) Zoomed-in view of the black dashed block in figure (C).

with the coding sequence of /11110000…/ for deflecting the THz beam to $\theta_r = 28.6°$. As shown in Fig. 4C, the external detector successfully detected the THz wave in the deflected direction. In Fig. 4D, the reaction time from the detection of the incident THz wave to the initiation of beam steering is within 3 s.

As displayed in Fig. 2C, each subarray can modulate its reflection amplitude by changing the VO$_2$ conductivity. Hence, the proposed SAM can adaptively control the reflected power by tuning the THz absorptivity of each subarray. In the second demonstration, we showed its ability to maintain power stability despite incident power fluctuation. A schematic of the experimental setup is shown in Fig. 5A. The SAM works in the IM state and self-adaptively adjusts the absorptivity on the basis of the detected signal. For this demonstration, we used a similar experimental setup as shown in Fig. 4A, except that θ_r is 15°, which is the specular angle corresponding to an incident angle of $\theta_i = 15°$. The sensor subarray is biased with 4 mA at 60°C for THz detection. Meanwhile, the modulation subarrays are biased with a current of 10 mA to reach the IM state. We set the

lower and upper V_{th} (V_{th1} and V_{th2}) and adjust the reflection coefficient of the modulation subarrays on the basis of the algorithm shown in Fig. 5B.

The reflected power measured by the external detector (blue) and the incident power detected by the SAM (orange) are plotted in Fig. 5C. As the external detector response increases from 200 μV to approximately 460 μV, the reflected power increases. When the software found that V_{sense} surpassed the V_{th2}, the host computer sent commands to SAM. Thus, the bias current of each modulation subarray is increased to reduce the THz reflectivity from R_H to R_L. The quantities of R_L and R_H indicated the THz reflectivity when the driving current is 10 and 0 mA, respectively. As a result, the reflected power dropped to 200 μV. When the SAM finds that V_{sense} is below the V_{th1}, the driving current is reduced from 10 to 0 mA to recover the reflectivity to R_H. Consequently, the reflected THz power went back. As shown in Fig. 5C, the reflected power remains constant most of the time, except for a short period after the switching (see movie S2).
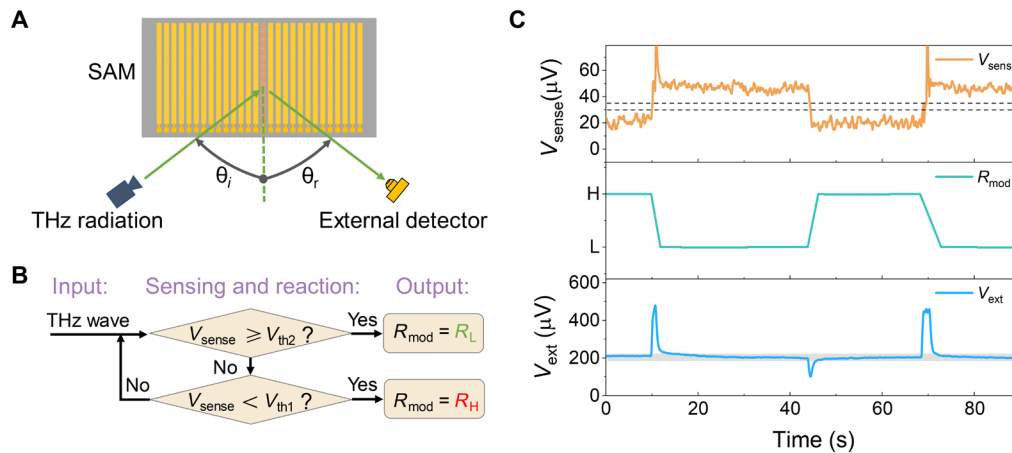
Fig. 5. Proof-of-concept demonstration of reflected THz power stabilization. (**A**) Schematic of adaptive stabilization of the reflected THz power. (**B**) Flowchart of the algorithm used to stabilize the THz power. (**C**) Incident power detected by the sensor subarray (orange), reflectivity of the modulation subarrays (cyan), and reflected THz signal measured by an external THz detector (blue) as a function of time.

DISCUSSION

Using the proposed SAM, we provide two conceptual demonstrations, suggesting their function of intelligent THz signal manipulation. In the first demonstration, the metasurface could decide whether to deflect the THz beam or go into standby mode to save power consumption. This self-adaptive beam steering feature can effectively eliminate coverage dead zones, making it suitable for large-scale deployment as RIS in the wireless communication network. The energy-saving option in our demonstration is a favorable plus for reducing operating costs. In the second demonstration, the metasurface could intelligently adjust the THz wave absorptivity according to the incident power. The power control capability is essential for device-to-device communication to suppress interference (*47*). In addition, on the basis of Fig. 2C, the SAM could achieve a significant attenuation or even perfect absorption of the incident THz wave, which can be used to improve communication security or reduce interference. Although the functionality demonstrated here is simple, more complicated and intelligent working modes can be realized after loading the appropriate software codes into the sensing reaction system according to the application requirement (*13–15*, *48–50*). Moreover, introducing a feedback loop into the future sensing reaction system will improve the accuracy and anti-interference capability of the control.

The proposed SAM does not require external detectors, unlike conventional intelligent metasurfaces at microwave frequencies. The unit cells with both modulation and detection functions effectively improve the integration of the intelligent metadevices. Thus, the device footprint and manufacturing costs can be effectively reduced. Furthermore, many materials, such as graphene (*34*, *35*), phase change materials (*36*, *37*), semiconductors (*21*, *38*), and superconductors (*51*, *52*), can be used for detectors and modulators with a similar design in a wide range of frequency bands. Thus, the idea is transferable and opens up a promising avenue for developing intelligent metasurfaces over a broad electromagnetic spectrum (see section S6 for more discussion).

In summary, we have developed a SAM in the THz region on the basis of the phase change material. The introduction of the unit cells with dual functions eliminates the need for the external sensor, thus offering a solution for highly integrated and low-cost metasurfaces and is transferable to other frequency bands. Two proof-to-concept demonstrations indicate that the SAM is capable of self-adaptive beam steering and power stabilization. It has intelligence as it can manipulate THz waves according to changes in the electromagnetic environment and application scenarios. Thus, it offers an excellent choice for RIS at THz frequencies for next-generation wireless communication and other information systems.

MATERIALS AND METHODS

Device fabrication and assembly

A 110-nm-thick VO_2 film was deposited on a 160-μm-thick *c*-cut sapphire substrate via pulsed laser deposition. After that, the positive photoresist (AZ1500) patterns were formed on the sample using ultraviolet photolithography. The patterns were transferred to the VO_2 film via reactive ion etching with a flow rate of 40 standard cubic centimeter per minute and a radio frequency power of 100 W. Next, 10-nm-thick titanium and 200-nm-thick gold films were deposited on the bottom surface of the substrate via magnetron sputtering. Then, the 10-nm-thick titanium and 200-nm-thick gold films were deposited on the top surface of the substrate after the second ultraviolet photolithography. Then, an array of bowtie antennas was formed on the top of the sample using the lift-off process. After device fabrication, the sample was attached to the thermal stage with the thermal paste as a thermally conductive layer. The sample was connected to a printed circuit board via wire bonding for electrical control. A detailed flow chart of the fabrication process is illustrated in fig. S1.

Beam steering measurement

An optical fiber–based THz time-domain spectroscopy system with a rotation stage was used to characterize the THz beam steering performance. The device was fixed at the center of the rotation stage. A transverse magnetic polarized THz beam generated from a THz emitter was incident to the sample at $\theta_i = 15°$. The angular distribution of the deflected THz signals was measured by a THz receiver fixed at the end of an arm of the rotation stage.

Coding sequence for beam deflection

When a plane wave illuminates a linear array at an incidence angle of θ_i, the array factor $f_A(\theta)$ based on array antenna theory can be expressed as follows

$$f_A(\theta) = \sum_{n=1}^{N} \Gamma_n e^{jnk_0 d_s(\sin\theta - \sin\theta_i)}$$
$$= \sum_{n=0}^{N/M} \sum_{m=1}^{M} \Gamma_m e^{j(nM+m)k_0 d_s(\sin\theta - \sin\theta_i)} \quad (2)$$

where Γ_n is the reflection coefficient of the n-th subarray, d_s is the subarray width, and M is the number of subarrays in the periodicity of the coding pattern. Equation 2 can be further derived as follows

$$f_A(\theta) = \sum_{m=1}^{M} \Gamma_m e^{jmk_0 d_s(\sin\theta - \sin\theta_i)} \sum_{n=0}^{N/M} e^{jnMk_0 d_s(\sin\theta - \sin\theta_i)} \quad (3)$$

Hence, the deflection angle should satisfy the following relationship

$$(\sin\theta_r - \sin\theta_i) = l\frac{\lambda}{Md_s} \quad (l = 0, \pm1, \pm2, \pm3\ldots) \quad (4)$$

where λ is the operating wavelength. In addition, the reflected field at θ_r is also dependent on the term $\sum_{m=1}^{M} \Gamma_m e^{jmk_0 d_s(\sin\theta - \sin\theta_i)}$.

When M is an even integer and 0 and 1 elements in a coding period are clustered, respectively, at both sides of the coding period [i.e., P8 (/00001111…/), P6 (/000111…/), and P4 (/0011…/)], the item can be denoted as follows

$$\sum_{m=1}^{M} \Gamma_m e^{jmk_0 d_s(\sin\theta - \sin\theta_i)} = \sum_{m=1}^{M} \Gamma_m e^{\frac{j2\pi ml}{M}}$$

$$= |\Gamma| \left(\sum_{m=1}^{\frac{M}{2}} e^{\frac{j2\pi ml}{M}} - e^{jl\pi} \sum_{m=1}^{\frac{M}{2}} e^{\frac{j2\pi ml}{M}} \right) \quad (5)$$

Here, the amplitude of the n-th subarray is represented by $|\Gamma|$, and the phase difference between the 0 and 1 elements is π. Hence, the complex reflection coefficients of the 0 and 1 elements are $|\Gamma|$ and $-|\Gamma|$, respectively. The first-order deflection beam ($l = 1$) is the primary deflection beam.

When a period of the coding sequence has an odd number of subarrays (M_0), such as P3 and P5, we form a coding sequence with $2M_0$ subarrays per period by alternating the coding periods with ($M_0 - 1$) and ($M_0 + 1$) elements. The deflection angle for different orders is calculated by substituting $M = 2M_0$ into Eq. 4. The second-order deflection angle ($l = 2$) corresponds to the predefined deflection angle. The first-order ($l = 1$) deflection beam is the unexpected beam appearing at a lower deflection angle.

THz responsivity measurement of the sensor subarray

To calculate the voltage responsivity of the sensor subarray, we measured the incident power at the focal spot using a THz power sensor (OPHIR, 3A-P-THz). The measured power density (P_{den}) is 0.42 mW/cm^2. The responsivity (R) is calculated using the following expression: $R = V_{out} / (P_{den}A)$, where V_{out} is the output voltage of the subarray and A is the subarray area. Therefore, on the basis of $V_{out} = 318.9\ \mu V$ shown in Fig. 3D and A is 0.4 mm by 14 mm for our SAM, the calculated R at a modulation frequency of 3.1 kHz is 13.6 V/W.

SUPPLEMENTARY MATERIALS

REFERENCES AND NOTES

1. T. Nagatsuma, G. Ducournau, C. C. Renaud, Advances in terahertz communications accelerated by photonics. *Nat. Photonics* **10**, 371–379 (2016).
2. S. Dang, O. Amin, B. Shihada, M.-S. Alouini, What should 6G be? *Nat. Electron.* **3**, 20–29 (2020).
3. S. Ummethala, T. Harter, K. Koehnle, Z. Li, S. Muehlbrandt, Y. Kutuvantavida, J. Kemal, P. Marin-Palomo, J. Schaefer, A. Tessmann, S. K. Garlapati, A. Bacher, L. Hahn, M. Walther, T. Zwick, S. Randel, W. Freude, C. Koos, THz-to-optical conversion in wireless communications using an ultra-broadband plasmonic modulator. *Nat. Photonics* **13**, 519–524 (2019).
4. S. Hu, F. Rusek, O. Edfors, Beyond massive MIMO: The potential of data transmission with large intelligent surfaces. *IEEE Trans. Signal Process.* **66**, 2746–2758 (2018).
5. C. Huang, A. Zappone, G. C. Alexandropoulos, M. Debbah, C. Yuen, Reconfigurable intelligent surfaces for energy efficiency in wireless communication. *IEEE Trans. Wireless Commun.* **18**, 4157–4170 (2019).
6. M. D. Renzo, A. Zappone, M. Debbah, M. S. Alouini, C. Yuen, J. D. Rosny, S. Tretyakov, Smart radio environments empowered by reconfigurable intelligent surfaces: How it works, state of research, and the road ahead. *IEEE J. Sel. Areas Commun.* **38**, 2450–2525 (2020).
7. L. Zhang, M. Z. Chen, W. Tang, J. Y. Dai, L. Miao, X. Y. Zhou, S. Jin, Q. Cheng, T. J. Cui, A wireless communication scheme based on space- and frequency-division multiplexing using digital metasurfaces. *Nat. Electron.* **4**, 218–227 (2021).
8. T. J. Cui, M. Q. Qi, X. Wan, J. Zhao, Q. Cheng, Coding metamaterials, digital metamaterials and programmable metamaterials. *Light Sci. Appl.* **3**, e218 (2014).
9. F. Liu, A. Pitilakis, M. S. Mirmoosa, O. Tsilipakos, X. Wang, A. C. Tasolamprou, S. Abadal, A. Cabellos-Aparicio, E. Alarcón, C. Liaskos, N. V. Kantartzis, M. Kafesaki, E. N. Economou, C. M. Soukoulis, S. Tretyakov, Programmable Metasurfaces: State of the Art and Prospects, in *2018 IEEE International Symposium on Circuits and Systems* (*ISCAS*) (2018) pp. 1–5.
10. L. Li, H. Zhao, C. Liu, L. Li, T. J. Cui, Intelligent metasurfaces: Control, communication and computing. *eLight* **2**, 7 (2022).
11. R. Zhu, J. Wang, T. Qiu, Y. Han, X. Fu, Y. Shi, X. Liu, T. Liu, Z. Zhang, Z. Chu, C.-W. Qiu, S. Qu, Remotely mind-controlled metasurface via brainwaves. *eLight* **2**, 10 (2022).
12. Q. Ma, W. Gao, Q. Xiao, L. Ding, T. Gao, Y. Zhou, X. Gao, T. Yan, C. Liu, Z. Gu, X. Kong, Q. H. Abbasi, L. Li, C.-W. Qiu, Y. Li, T. J. Cui, Directly wireless communication of human minds via non-invasive brain-computer-metasurface platform. *eLight* **2**, 11 (2022).
13. Q. Ma, G. D. Bai, H. B. Jing, C. Yang, L. Li, T. J. Cui, Smart metasurface with self-adaptively reprogrammable functions. *Light: Sci. Appl.* **8**, 98 (2019).
14. C. Qian, B. Zheng, Y. Shen, L. Jing, E. Li, L. Shen, H. Chen, Deep-learning-enabled self-adaptive microwave cloak without human intervention. *Nat. Photonics* **14**, 383–390 (2020).
15. L. Li, H. Ruan, C. Liu, Y. Li, Y. Shuang, A. Alu, C. W. Qiu, T. J. Cui, Machine-learning reprogrammable metasurface imager. *Nat. Commun.* **10**, 1082 (2019).
16. M. Mercuri, I. R. Lorato, Y.-H. Liu, F. Wieringa, C. V. Hoof, T. Torfs, Vital-sign monitoring and spatial tracking of multiple people using a contactless radar-based sensor. *Nat. Electron.* **2**, 252–262 (2019).
17. H. P. Wang, Y. B. Li, H. Li, J. L. Shen, S. Y. Dong, S. Y. Wang, K. N. Qi, Q. Ma, S. Jin, S. J. Li, T. J. Cui, Intelligent metasurface with frequency recognition for adaptive manipulation of electromagnetic wave. *Nanophotonics* **11**, 1401–1411 (2022).
18. H. P. Wang, Y. X. Zhou, H. Li, G. D. Liu, S. M. Yin, P. J. Li, S. Y. Dong, C. Y. Gong, S. Y. Wang, Y. B. Li, T. J. Cui, Noncontact electromagnetic wireless recognition for prosthesis based on intelligent metasurface. *Adv. Sci.* **9**, 2105056 (2022).
19. S. Koenig, D. Lopez-Diaz, J. Antes, F. Boes, R. Henneberger, A. Leuther, A. Tessmann, R. Schmogrow, D. Hillerkuss, R. Palmer, T. Zwick, C. Koos, W. Freude, O. Ambacher, J. Leuthold, I. Kallfass, Wireless sub-THz communication system with high data rate. *Nat. Photonics* **7**, 977–981 (2013).
20. P. C. Wu, R. A. Pala, G. Kafaie Shirmanesh, W. H. Cheng, R. Sokhoyan, M. Grajower, M. Z. Alam, D. Lee, H. A. Atwater, Dynamic beam steering with all-dielectric electro-optic III-V multiple-quantum-well metasurfaces. *Nat. Commun.* **10**, 3654 (2019).
21. H. T. Chen, W. J. Padilla, M. J. Cich, A. K. Azad, R. D. Averitt, A. J. Taylor, A metamaterial solid-state terahertz phase modulator. *Nat. Photonics* **3**, 148–151 (2009).
22. Q. Wang, E. T. F. Rogers, B. Gholipour, C.-M. Wang, G. Yuan, J. Teng, N. I. Zheludev, Optically reconfigurable metasurfaces and photonic devices based on phase change materials. *Nat. Photonics* **10**, 60–65 (2016).
23. M. R. Hashemi, S. H. Yang, T. Wang, N. Sepulveda, M. Jarrahi, Electronically-controlled beam-steering through vanadium dioxide metasurfaces. *Sci. Rep.* **6**, 35439 (2016).
24. B. Chen, J. Wu, W. Li, C. Zhang, K. Fan, Q. Xue, Y. Chi, Q. Wen, B. Jin, J. Chen, P. Wu, Programmable terahertz metamaterials with non-volatile memory. *Laser Photonics Rev.* **16**, 2100472 (2022).
25. X. Duan, S. T. White, Y. Cui, F. Neubrech, Y. Gao, R. F. Haglund, N. Liu, Reconfigurable multistate optical systems enabled by VO$_2$ phase transitions. *ACS Photonics* **7**, 2958–2965 (2020).
26. G. Perez-Palomino, M. Barba, J. A. Encinar, R. Cahill, R. Dickie, P. Baine, M. Bain, Design and demonstration of an electronically scanned reflectarray antenna at 100 GHz using multiresonant cells based on liquid crystals. *IEEE Trans. Antennas Propag.* **63**, 3722–3727 (2015).

27. J. Wu, Z. Shen, S. Ge, B. Chen, Z. Shen, T. Wang, C. Zhang, W. Hu, K. Fan, W. Padilla, Y. Lu, B. Jin, J. Chen, P. Wu, Liquid crystal programmable metasurface for terahertz beam steering. *Appl. Phys. Lett.* **116**, 131104 (2020).

28. J. Li, P. Yu, S. Zhang, N. Liu, Electrically-controlled digital metasurface device for light projection displays. *Nat. Commun.* **11**, 3574 (2020).

29. C. X. Liu, F. Yang, X. J. Fu, J. W. Wu, L. Zhang, J. Yang, T. J. Cui, Programmable manipulations of terahertz beams by transmissive digital coding metasurfaces based on liquid crystals. *Adv. Opt. Mater.* **9**, 2100932 (2021).

30. M. A. Naveed, J. Kim, I. Javed, M. A. Ansari, J. Seong, Y. Massoud, T. Badloe, I. Kim, K. Riaz, M. Zubair, M. Q. Mehmood, J. Rho, Novel spin-decoupling strategy in liquid crystal-integrated metasurfaces for interactive metadisplays. *Adv. Opt. Mater.* **10**, 2200196 (2022).

31. M. Tamagnone, S. Capdevila, A. Lombardo, J. Wu, A. Zurutuza, A. Centeno, A. Ionescu, A. Ferrari, J. Mosig, Graphene reflectarray metasurface for terahertz beam steering and phase modulation. arXiv:1806.02202 (2018).

32. E. Carrasco, J. Perruisseau-Carrier, Reflectarray antenna at terahertz using graphene. *IEEE Antennas Wirel. Propag. Lett.* **12**, 253–256 (2013).

33. R. A. Lewis, A review of terahertz detectors. *J. Phys. D Appl. Phys.* **52**, 433001 (2019).

34. S. H. Lee, M. Choi, T.-T. Kim, S. Lee, M. Liu, X. Yin, H. K. Choi, S. S. Lee, C.-G. Choi, S.-Y. Choi, X. Zhang, B. Min, Switching terahertz waves with gate-controlled active graphene metamaterials. *Nat. Mater.* **11**, 936–941 (2012).

35. M. Mittendorff, S. Winnerl, J. Kamann, J. Eroms, D. Weiss, H. Schneider, M. Helm, Ultrafast graphene-based broadband THz detector. *Appl. Phys. Lett.* **103**, 021113 (2013).

36. M. Seo, J. Kyoung, H. Park, S. Koo, H.-s. Kim, H. Bernien, B. J. Kim, J. H. Choe, Y. H. Ahn, H.-T. Kim, N. Park, Q. H. Park, K. Ahn, D.-s. Kim, Active terahertz nanoantennas based on VO₂ phase transition. *Nano Lett.* **10**, 2064–2068 (2010).

37. C. H. Chen, X. J. Yi, X. R. Zhao, B. F. Xiong, Characterizations of VO₂-based uncooled microbolometer linear array. *Sens. Actuators A* **90**, 212–214 (2001).

38. M. S. Vitiello, D. Coquillat, L. Viti, D. Ercolani, F. Teppe, A. Pitanti, F. Beltram, L. Sorba, W. Knap, A. Tredicucci, Room-temperature terahertz detectors based on semiconductor nanowire field-effect transistors. *Nano Lett.* **12**, 96–101 (2012).

39. C. Zhang, G. Zhou, J. Wu, Y. Tang, Q. Wen, L. Shaoxian, J. Han, B. Jin, J. Chen, P. Wu, Active control of terahertz waves using vanadium-dioxide-embedded metamaterials. *Phys. Rev. Appl.* **11**, 054016 (2019).

40. A. Sharoni, J. G. Ramirez, I. K. Schuller, Multiple avalanches across the metal-insulator transition of vanadium oxide nanoscaled junctions. *Phys. Rev. Lett.* **101**, 026404 (2008).

41. R. Lu, Z. Li, G. Xu, J. Z. Wu, Suspending single-wall carbon nanotube thin film infrared bolometers on microchannels. *Appl. Phys. Lett.* **94**, 163110 (2009).

42. C. Caloz, T. Itoh, *Electromagnetic Metamaterials:Transmission Line Theory and Microwave Applications* (John Wiley & Sons, 2005).

43. L. Fu, H. Schweizer, H. Guo, N. Liu, H. Giessen, Synthesis of transmission line models for metamaterial slabs at optical frequencies. *Phys. Rev. B* **78**, 115110 (2008).

44. N. Yu, P. Genevet, M. A. Kats, F. Aieta, J. P. Tetienne, F. Capasso, Z. Gaburro, Light propagation with phase discontinuities: Generalized laws of reflection and refraction. *Science* **334**, 333–337 (2011).

45. V. John, *Antenna Engineering Handbook* (McGraw-Hill Professional, ed. 4, 2007).

46. X. Tu, P. Xiao, L. Kang, C. Jiang, X. Guo, Z. Jiang, R. Su, X. Jia, J. Chen, P. Wu, Nb₅N₆ microbolometer for sensitive, fast-response, 2-μm detection. *Opt. Express* **26**, 15585–15593 (2018).

47. R. Liu, Q. Wu, M. D. Renzo, Y. Yuan, A path to smart radio environments: An industrial viewpoint on reconfigurable intelligent surfaces. *IEEE Wireless Commun.* **29**, 202–208 (2022).

48. L. Li, Y. Shuang, Q. Ma, H. Li, H. Zhao, M. Wei, C. Liu, C. Hao, C.-W. Qiu, T. J. Cui, Intelligent metasurface imager and recognizer. *Light Sci. Appl.* **8**, 97 (2019).

49. C. Liu, Q. Ma, Z. J. Luo, Q. R. Hong, Q. Xiao, H. C. Zhang, L. Miao, W. M. Yu, Q. Cheng, L. Li, T. J. Cui, A programmable diffractive deep neural network based on a digital-coding metasurface array. *Nat. Electron.* **5**, 113–122 (2022).

50. M. A. Abbas, J. Kim, A. S. Rana, I. Kim, B. Rehman, Z. Ahmad, Y. Massoud, J. Seong, T. Badloe, K. Park, M. Q. Mehmood, M. Zubair, J. Rho, Nanostructured chromium-based broadband absorbers and emitters to realize thermally stable solar thermophotovoltaic systems. *Nanoscale* **14**, 6425–6436 (2022).

51. S. Ariyoshi, C. Otani, A. Dobroiu, H. Sato, K. Kawase, H. M. Shimizu, T. Taino, H. Matsuo, Terahertz imaging with a direct detector based on superconducting tunnel junctions. *Appl. Phys. Lett.* **88**, 203503 (2006).

52. C. Li, J. Wu, S. Jiang, R. Su, C. Zhang, C. Jiang, G. Zhou, B. Jin, L. Kang, W. Xu, J. Chen, P. Wu, Electrical dynamic modulation of THz radiation based on superconducting metamaterials. *Appl. Phys. Lett.* **111**, 092601 (2017).

53. Y. Yang, O. D. Gurbuz, G. M. Rebeiz, An eight-element 370–410-GHz phased-array transmitter in 45-nm CMOS SOI with peak EIRP of 8–8.5 dBm. *IEEE Trans. Microwave Theory Tech.* **64**, 4241–4249 (2016).

54. Y. Tousi, E. Afshari, A high-power and scalable 2-D phased array for terahertz CMOS integrated systems. *IEEE J. Solid-State Circuits* **50**, 597–609 (2015).

55. R. Han, C. Jiang, A. Mostajeran, M. Emadi, H. Aghasi, H. Sherry, A. Cathelin, E. Afshari, A SiGe terahertz heterodyne imaging transmitter With 3.3 mW radiated power and fully-integrated phase-locked loop. *IEEE J. Solid-State Circuits* **50**, 2935–2947 (2015).

56. N. J. Karl, R. W. McKinney, Y. Monnai, R. Mendis, D. M. Mittleman, Frequency-division multiplexing in the terahertz range using a leaky-wave antenna. *Nat. Photonics* **9**, 717–720 (2015).

57. H. Matsumoto, I. Watanabe, A. Kasamatsu, Y. Monnai, Integrated terahertz radar based on leaky-wave coherence tomography. *Nat. Electron.* **3**, 122–129 (2020).

58. Y. Ghasempour, R. Shrestha, A. Charous, E. Knightly, D. M. Mittleman, Single-shot link discovery for terahertz wireless networks. *Nat. Commun.* **11**, 2017 (2020).

59. Z. Chen, X. Chen, L. Tao, K. Chen, M. Long, X. Liu, K. Yan, R. I. Stantchev, E. Pickwell-MacPherson, J.-B. Xu, Graphene controlled Brewster angle device for ultra broadband terahertz modulation. *Nat. Commun.* **9**, 4909 (2018).

60. J. Cai, B. Chen, J. Wu, Y.-H. Li, Q. Xue, T. Wang, C. Zhang, Q. Wen, B. Jin, J. Chen, P. Wu, Reconfigurable terahertz rainbow deflector. *Appl. Phys. Lett.* **118**, 141105 (2021).

61. M. Dyakonov, M. Shur, Detection, mixing, and frequency multiplication of terahertz radiation by two-dimensional electronic fluid. *IEEE Trans. Electron Devices* **43**, 380–387 (1996).

62. J. D. Sun, Y. F. Sun, D. M. Wu, Y. Cai, H. Qin, B. S. Zhang, High-responsivity, low-noise, room-temperature, self-mixing terahertz detector realized using floating antennas on a GaN-based field-effect transistor. *Appl. Phys. Lett.* **100**, 013506 (2012).

63. P. Hillger, J. Grzyb, R. Jain, U. R. Pfeiffer, Terahertz imaging and sensing applications with silicon-based technologies. *IEEE Trans. Terahertz Sci. Technol.* **9**, 1–19 (2019).

64. T. Kleine-Ostmann, P. Dawson, K. Pierz, G. Hein, M. Koch, Room-temperature operation of an electrically driven terahertz modulator. *Appl. Phys. Lett.* **84**, 3555–3557 (2004).

65. Y. Zhang, S. Qiao, S. Liang, Z. Wu, Z. Yang, Z. Feng, H. Sun, Y. Zhou, L. Sun, Z. Chen, X. Zou, B. Zhang, J. Hu, S. Li, Q. Chen, L. Li, G. Xu, Y. Zhao, S. Liu, Gbps terahertz external modulator based on a composite metamaterial with a double-channel heterostructure. *Nano Lett.* **15**, 3501–3506 (2015).

66. S. Venkatesh, X. Lu, H. Saeidi, K. Sengupta, A high-speed programmable and scalable terahertz holographic metasurface based on tiled CMOS chips. *Nat. Electron.* **3**, 785–793 (2020).

67. C. Chen, X. Yi, J. Zhang, X. Zhao, Linear uncooled microbolometer array based on VOₓ thin films. *Infrared Phys. Technol.* **42**, 87–90 (2001).

68. S. Vadnala, N. Paul, A. Agrawal, S. G. Singh, Enhanced infrared sensing properties of vanadium pentoxide nanofibers for bolometer application. *Mater. Sci. Semicond. Process.* **81**, 82–88 (2018).

69. X. Chen, X. Yi, VO₂-based microbolometer uncooled infrared focal plane arrays with CMOS readout integrated circuit, in *Asia-Pacific Optical Communications* (SPIE, 2005), vol. 6020 p. 602032.

70. Z. Zhu, P. G. Evans, R. F. Haglund, J. G. Valentine, Dynamically reconfigurable metadevice employing nanostructured phase-change materials. *Nano Lett.* **17**, 4881–4885 (2017).

71. Y. Kim, P. C. Wu, R. Sokhoyan, K. Mauser, R. Glaudell, G. K. Shirmanesh, H. A. Atwater, Phase modulation with electrically tunable vanadium dioxide phase-change metasurfaces. *Nano Lett.* **19**, 3961–3968 (2019).

72. F. H. Koppens, T. Mueller, P. Avouris, A. C. Ferrari, M. S. Vitiello, M. Polini, Photodetectors based on graphene, other two-dimensional materials and hybrid systems. *Nat. Nanotechnol.* **9**, 780–793 (2014).

73. M. S. Ergoktas, G. Bakan, E. Kovalska, L. W. Le Fevre, R. P. Fields, P. Steiner, X. Yu, O. Salihoglu, S. Balci, V. I. Fal'ko, K. Novoselov, R. A. W. Dryfe, C. Kocabas, Multispectral graphene-based electro-optical surfaces with reversible tunability from visible to microwave wavelengths. *Nat. Photonics* **15**, 493–498 (2021).